Magnon-magnon interaction and magnon relaxation time in a ferromagnetic $Cr_2Ge_2Te_6$ monolayer

Ke Wang,[1,2] Xiansong Xu,[3] Yuan Cheng,[2] Min Zhang,[1] Jian-Sheng Wang,[4] Hai Wang,[1,*] and Gang Zhang[2,†]

[1]*Xidian University, No. 2 Taibai Road, Xi'an, Shaanxi Province 710071, China*

[2]*Institute of High Performance Computing, A*STAR, 138632, Singapore*

[3]*Science, Mathematics and Technology Cluster, Singapore University of Technology and Design, 487372, Singapore*

[4]*Department of Physics, National University of Singapore, 117551, Singapore*

(Received 9 September 2020; revised 30 November 2020; accepted 15 December 2020; published 29 December 2020)

Despite the intense amount of attention and huge potential of two-dimensional (2D) magnets for applications in novel magnetic, magneto-optical, magnetothermal, and magnetoelectronic devices, there is a lack of robust strategy developed to systematically understand magnon-magnon interactions (MMIs) at finite temperature. In this paper, we present a first-principles theoretical method to introduce the finite temperature magnon-magnon interaction into a Heisenberg Hamiltonian through a correction energy. Wick's theorem is used to decouple the four-magnon operators to two-magnon order. We demonstrate the capabilities of this method by studying the strength of MMI in a $Cr_2Ge_2Te_6$ monolayer. The spin-wave spectrum at finite temperature and the time-dependent spin autocorrelation function are explored. It is found that the magnon relaxation time due to magnon-magnon scattering increases with temperature because of the reduction in magnon energy, while it decreases with wave vector and external magnetic field. Our results provide insight into understanding the magnon damping and energy dissipation in two-dimensional ferromagnetic materials.

DOI: 10.1103/PhysRevB.102.235434

I. INTRODUCTION

The two-dimensional (2D) materials exfoliated from various bulk van der Waals (vdW) sheets attract substantial attention in materials science, condensed matter physics, and electronic engineering, because of their fascinating properties [1–4]. Although all major electronic classes (metals, insulators, and semiconductors) have been observed in 2D materials [5–7], a 2D magnet was missing until the discovery of intrinsic ferromagnetism in Cr trihalide and chalcogenides in 2017 [8,9]. Subsequently, numerous 2D magnets with long-range order have been discovered and investigated, such as $Fe_{5-x}GeTe_2$ [10,11], XPS_3 (X = Mn, Fe) [12–16], $CrPS_4$ [17], Cr_2S_3 [18,19], $CoGa_2X_4$ (X = S, Se, Te) [20], XH_2 (X = Sc, Ti, V, Cr, Fe, Co, Ni) [21], $CrOX$ (X = Cl, Br) [22,23], non-vdW transition-metal oxides [24], and some 2D transition-metal carbides and nitrides (MXenes) [25,26].

In the family of 2D magnets, the characteristic of magnetic anisotropy is quite distinct [27–29]. For instance, in monolayer CrI_3, the magnetic anisotropy parameter is ∼29.3% of the exchange constant, revealing strong magnetic anisotropy energy [30]. For monolayer $Cr_2Ge_2Te_6$, the magnetic anisotropy parameter is only 2% of the nearest-neighboring exchange constant, so that the magnetic anisotropy is ignorable [31]. Based on the magnetic exchange interaction and the magnetic anisotropy, the Curie/Néel temperature can be calculated using the mean-field theory [32,33]. Meantime, several studies have been implemented to enhance the Curie/Néel temperature for the application of 2D magnets in magneto-optical, magnetothermal, and magnetoelectronic devices by functionalization [34–36], external field [8,37], and strain [8,38,39]. Below the Curie/Néel temperature, the time-resolved magneto-optical Kerr effect (TR MOKE) and the time-resolved Faraday rotation (TRFR) are often employed to investigate the magnetic-optical coupling [9,31,40], demonstrating the rich magnetic behaviors in 2D magnets. The Hall effect (including spin Hall effect, anomalous Hall effect, and thermal Hall effect) in 2D magnets also attracts substantial attention, which not only promotes the development of novel Hall devices but also provides a new route to detect the existence of magnetism [41–45]. Among these Hall effects, the thermal Hall effect is related to the coupling between spin waves and lattice vibration (magnon-phonon coupling) [46] usually studied by Raman spectra [47,48], phonon spectrum [49,50], and spin-wave spectrum [51,52]. In spintronics, the manipulation of magnetic order also is a hot topic, and there are numerous manipulation strategies, such as stack [53,54], electrostatic doping [55,56], and pressure [57,58]. In addition, Hofmann explored the temperature dependence of two-dimensional ideal ferromagnets when temperature is 1% of the exchange constant [59,60]. So far, despite intense studies in this area, there still is a lack of robust theoretical methods for studying the magnon-magnon interaction (MMI) at finite temperature, which is crucial for coherent spintronics.

In this paper, we introduce the dynamical interaction arising from the change in magnon population caused by temperature into a Heisenberg Hamiltonian to describe the spin-wave spectrum of a $Cr_2Ge_2Te_6$ (CGT) monolayer at finite temperature. The influence of dynamical interaction on magnon dispersion can be regarded as a correction term

*wanghai@mail.xidian.edu.cn

†zhangg@ihpc.a-star.edu.sg

caused by the decoupling of the products of four Bose operators. To observe the MMI, the time-dependent spin autocorrelation is employed, and the relaxation time τ_{MM} is obtained by fitting the spin autocorrelation with an exponential function. We theoretically find the relaxation time τ_{MM} (contributed by MMI) increases with temperature but decreases remarkably with the external magnetic field. Our results shed light on the understanding of dissipation of magnon energy at finite temperature.

II. THEORETICAL MODELS AND COMPUTATIONAL DETAILS

Here, the 2D ferromagnetic system is described by

$$H = -\frac{1}{2}\sum_{\substack{l,f\in N\\ l\neq f}} J_{lf}\boldsymbol{S}_l\cdot\boldsymbol{S}_f - \sum_l g\mu_B\boldsymbol{B}\cdot\boldsymbol{S}_l + H_{\mathrm{an}} + H_{\mathrm{d}}, \quad (1)$$

where the first term represents isotropic exchange interaction, the second term is Zeeman energy, and the last two terms describe the magnetic anisotropy (H_{an}) and dipole-dipole interaction (H_{d}), respectively. Recently, Shen demonstrated that the magnetic dipole-dipole interaction leads to a small modification in magnon frequencies [61]. This modification is very small for the CGT monolayer (about -0.15 meV/u.c.) ("u.c." means "unit cell"); thus it is ignorable comparing with the exchange interaction ($\sim$6.37 meV/u.c.) in the CGT monolayer [31].

In Eq. (1), H_{an} can be calculated by

$$H_{\mathrm{an}} = -\sum_{\substack{l,f\\ l\neq f}} A_{lf}S_l^zS_f^z, \quad (2)$$

where A_{lf} is the anisotropy parameter along the z axis. At present, there are two methods to estimate the anisotropy parameter: the *XXZ* model and the Kitaev interaction model. For the *XXZ* model, the off-diagonal elements of the exchange constant matrix are neglected, and then the anisotropy parameter is obtained by difference between the exchange constants for the x (J^{xx}) and z axes (J^{zz}). When the Kitaev interaction is considered, it is necessary to diagonalize the exchange constant matrix, and the diagonal elements are represented by J^{α}, J^{β}, and J^{γ}. Subsequently, the anisotropy parameter is also estimated by

$$A_{lf} = J_{lf}^{\gamma} - \tfrac{1}{2}\left(J_{lf}^{\alpha} + J_{lf}^{\beta}\right). \quad (3)$$

In Ref. [29], both methods are used to calculate the anisotropy parameter of the CGT monolayer, and the anisotropy parameters are 0.1–0.2 meV and 0.36 meV by the *XXZ* model and the Kitaev interaction model, respectively. These values are much smaller than the nearest-neighbor exchange constant of the CGT monolayer ($\sim$6.64 meV), unlike that in the CrI_3 monolayer (anisotropy parameter is 0.85 meV while $J = 2.44$ meV) [29]. This indicates that in CGT the anisotropy parameter is only 1%–5% of the exchange constant, while this ratio is 30% in CrI_3. Therefore, the Heisenberg model is applicable to the CGT monolayer, in which the anisotropic parameter is zero.

The magnetic anisotropy can be directly evaluated by the magnetocrystalline magnetic anisotropy energy (CMAE), which is defined as the energy difference between in-plane and out-of-plane spin configurations. For the CGT monolayer, there are some controversies regarding its easy axis. Zhang *et al.* showed the CGT monolayer has an out-of-plane easy-axis [50], but Fang *et al.* [31] and Xu *et al.* [29] showed that the easy axis of the CGT monolayer is the in-plane direction while that of multilayer is the out-of-plane direction. To determine the CMAE of the CGT monolayer, we performed first-principles based self-consistent calculations considering spin-orbit coupling. The energies for the in-plane and out-of-plane magnetizations in the CGT monolayer were obtained as -49.0513 eV/u.c. and -49.0510 eV/u.c. Then the CMAE is -0.3 meV revealing the in-plane easy axis, which agrees well with the conclusions of Fang *et al.* and Xu *et al.*. Overall, the magnetic anisotropy is slight in monolayer CGT and the term (H_{an}) in Eq. (1) can be ignored, as also adopted in previous works in the literature [31,50].

The Heisenberg Hamiltonian omitting the magnetic anisotropy and dipole-dipole interaction for a CGT monolayer is shown as follows:

$$H = -\frac{1}{2}\sum_{\substack{l,f\in N\\ l\neq f}} J\boldsymbol{S}_l\cdot\boldsymbol{S}_f - \sum_l g\mu_B\boldsymbol{B}\cdot\boldsymbol{S}_l. \quad (4)$$

For a given magnetic lattice, $\boldsymbol{S} = (S^x, S^y, S^z)$ is the spin vector whose amplitude is S_0. J is the isotropic exchange constant. In this work, only the nearest-neighbor interaction is taken into account, because the second-nearest-neighbor and third-nearest-neighbor exchange constants of the CGT monolayer are about -0.045 and 0.15 meV per unit cell, which are much lower than the nearest-neighbor exchange constant (6.37 meV) [31]. Therefore, for simplification, we only consider one exchange coupling parameter. This simplification was also adopted in previous works in the literature [33,50]. The Landé factor is represented as g, μ_B is the Bohr magneton, and $\boldsymbol{B}$ represents an external magnetic field along the c axis. Without loss of generality, the equilibrium magnetization is assumed to be parallel to the external field. In addition, transverse components $S^{\pm} = S^x \pm iS^y$ are defined to eliminate the dependence between S^x and S^y. According to the Holstein-Primakoff (HP) approximation [62,63], $S^{\pm}$ and S^z for a given site can be written as

$$S^+ = (\sqrt{2S_0 - a^+a})a, \quad S^- = a^+(\sqrt{2S_0 - a^+a}),$$
$$S^z = (S_0 - a^+a), \quad (5)$$

where a^+ and a are the creation and annihilation operators of magnon for the given site, respectively. The operators of the magnon described in coordinate space are transferred into reciprocal space by the Fourier transform:

$$a_k = N^{-\frac{1}{2}}\sum_{\boldsymbol{r}} e^{-i\boldsymbol{k}\cdot\boldsymbol{r}}a, \quad a_k^+ = N^{-\frac{1}{2}}\sum_{\boldsymbol{r}} e^{i\boldsymbol{k}\cdot\boldsymbol{r}}a^+, \quad (6)$$

where $\boldsymbol{k}$ is the wave vector, $\boldsymbol{r}$ is the position vector of the lattice point, and N is the number of unit cells in the supercell. The magnon density $\langle a_k^+a_k\rangle$ can be calculated by the Bose-Einstein distribution function:

$$\langle a_k^+a_k\rangle = \frac{1}{(e^{\hbar\omega_k/k_BT} - 1)}, \quad (7)$$

with Boltzmann constant k_B and the reduced Planck constant $\hbar$. At low temperature (close to zero), $\hbar w/k_BT$ tends to be infinite, resulting in an ignorable $\langle a_k^+ a_k\rangle$. With temperature increases, $\langle a_k^+ a_k\rangle$ increases significantly, and thus cannot be ignored.

A. Zero temperature model

For completeness, firstly we introduce the spin-wave spectrum model at zero temperature, at which the population of excited magnon is low; therefore the magnon density can be negligible with respect to $2S_0$ [64,65]. The transverse components of spin vector for a given site can be rewritten as

$$S^+ = (\sqrt{2S_0 - a^+a})a \approx (\sqrt{2S_0})a,$$
$$S^- = (\sqrt{2S_0 - a^+a})a^+ \approx a^+(\sqrt{2S_0}). \quad (8)$$

The Hamiltonian can be given as

$$H = H_0 + H_B = -\frac{1}{2}J \sum_{\substack{l,f\in N\\ l\neq f}} [(S_0 - a_l^+a_l)(S_0 - a_f^+a_f) + S_0(a_la_f^+ + a_l^+a_f)] - \sum_l g\mu_B B(S_0 - a_l^+a_l), \quad (9)$$

Here H_0 and H_B are

$$H_0 = -\frac{1}{2}J \sum_{\substack{l,f\in N\\ l\neq f}} [(S_0 - a_l^+a_l)(S_0 - a_f^+a_f) + S_0(a_la_f^+ + a_l^+a_f)], \quad (10)$$

$$H_B = -\sum_l g\mu_B B(S_0 - a_l^+a_l). \quad (11)$$

Following Eq. (6), Eq. (9) can be transferred into the reciprocal space. Then, the Hamiltonian in the reciprocal space can be written as

$$H = H_0 + H_B = -\frac{1}{2}J \sum_{\substack{l,f\in N\\ l\neq f}} \left[S_0^2 - S_0N^{-1}\sum_k \left(a_{l,k}^+a_{l,k} + a_{f,k}^+a_{f,k} - a_{f,k}^+a_{l,k}\gamma_k - a_{l,k}^+a_{f,k}\gamma_k\right)\right] - \sum_l g\mu_B B\left(S_0 - N^{-1}\sum_k a_{l,k}^+a_{l,k}\right), \quad (12)$$

with $\gamma_k = \frac{1}{Z}\sum_{l,\ f\ \in N} e^{ik\cdot(r_f - r_l)}$. Z is the coordination number for the nearest-neighbor exchange interaction.

In each unit cell of monolayer CGT, it includes two magnetic Cr^{3+} ions; then the Hamiltonian is

$$H = H_0 + H_B = E_0 + \sum_k \hbar\omega_k^{\pm} a_k^+a_k = E_0 + \sum_k [JZS_0(1 \pm \gamma_k) + 2g\mu_B B]a_k^+a_k, \quad (13)$$

where E_0 is the energy of the ground state:

$$E_0 = -2NJZS_0 - 2Ng\mu_B BS_0. \quad (14)$$

The frequencies for optical ($\hbar w^+$) and acoustic ($\hbar w^-$) magnons can be obtained by

$$\hbar\omega_k^{\pm} = E_{\mathrm{SI}}^{\pm} + 2g\mu_B B = JZS_0(1 \pm \gamma_k) + 2g\mu_B B, \quad (15)$$

with the isotropic exchange constant J. $E_{\mathrm{SI}}^{\pm}$ is called "static interaction," which describes the magnetic exchange interaction at zero temperature (without perturbation) [66].

B. Magnon-magnon interaction at finite temperature

From Eq. (7), it is obvious that the magnon density increases with temperature because of the excitation of substantial magnons, so that at finite temperature the transverse components of spin vector for a given site should be written as follows [67]:

$$S^+ = (\sqrt{2S_0 - a^+a})a \approx \sqrt{2S_0}\left(1 - \frac{a^+a}{4S_0}\right)a, \quad S^- = a^+(\sqrt{2S_0 - a^+a}) \approx a^+\sqrt{2S_0}\left(1 - \frac{a^+a}{4S_0}\right). \quad (16)$$

Then, the higher order terms appear in the Heisenberg Hamiltonian:

$$H(T) \approx H_0 + H_B - \frac{1}{2}J \sum_{\substack{l,f\in N\\ l\neq f}} \left[a_l^+a_la_f^+a_f + \frac{a_l^+a_la_l^+a_f^+}{4} + \frac{a_f^+a_fa_l^+a_f^+}{4} + \frac{a_l^+a_fa_l^+a_l}{4} + \frac{a_l^+a_fa_f^+a_f}{4}\right]. \quad (17)$$

Next, the normal coordinate is introduced into the Hamiltonian by Eq. (6), and the Fourier transform for the four-order terms is shown as following:

$$a_l^+a_la_f^+a_f = N^{-2}\sum_{k-q} e^{-i(k-q)\mathbf{r}_l}a_{k-q}^+ \sum_k e^{ik\mathbf{r}_f}a_k \sum_{k'+q} e^{-i(k'+q)\mathbf{r}_f}a_{k'+q}^+ \sum_{k'} e^{ik'\mathbf{r}_l}a_{k'} = N^{-2}\sum_{k,k',q} \gamma_{k-k'-q}a_{k-q}^+a_{k'+q}^+a_{k'}a_k, \quad (18)$$

$$a_l^+ a_l a_l a_f^+ = N^{-2} \sum_{k-q} e^{-i(k-q)\boldsymbol{r}_f} a_{k-q}^+ \sum_k e^{ik\boldsymbol{r}_l} a_k \sum_{k'+q} e^{-i(k'+q)\boldsymbol{r}_l} a_{k'+q}^+ \sum_{k'} e^{ik'\boldsymbol{r}_l} a_{k'} = N^{-2} \sum_{k,k',q} \gamma_{k-q} a_{k-q}^+ a_{k'+q}^+ a_{k'} a_k, \tag{19}$$

$$a_f^+ a_f a_l a_f^+ = N^{-2} \sum_{k-q} e^{-i(k-q)\boldsymbol{r}_f} a_{k-q}^+ \sum_k e^{ik\boldsymbol{r}_f} a_k \sum_{k'+q} e^{-i(k'+q)\boldsymbol{r}_f} a_{k'+q}^+ \sum_{k'} e^{ik'\boldsymbol{r}_l} a_{k'} = N^{-2} \sum_{k,k',q} \gamma_{k'} a_{k-q}^+ a_{k'+q}^+ a_{k'} a_k, \tag{20}$$

$$a_l^+ a_f a_l^+ a_l = N^{-2} \sum_{k-q} e^{-i(k-q)\boldsymbol{r}_l} a_{k-q}^+ \sum_k e^{ik\boldsymbol{r}_l} a_k \sum_{k'+q} e^{-i(k'+q)\boldsymbol{r}_l} a_{k'+q}^+ \sum_{k'} e^{ik'\boldsymbol{r}_f} a_{k'} = N^{-2} \sum_{k,k',q} \gamma_{k'} a_{k-q}^+ a_{k'+q}^+ a_{k'} a_k, \tag{21}$$

$$a_l^+ a_f a_f^+ a_f = N^{-2} \sum_{k-q} e^{-i(k-q)\boldsymbol{r}_l} a_{k-q}^+ \sum_k e^{ik\boldsymbol{r}_f} a_k \sum_{k'+q} e^{-i(k'+q)\boldsymbol{r}_f} a_{k'+q}^+ \sum_{k'} e^{ik'\boldsymbol{r}_f} a_{k'} = N^{-2} \sum_{k,k',q} \gamma_{k-q} a_{k-q}^+ a_{k'+q}^+ a_{k'} a_k. \tag{22}$$

Then, the Hamiltonian at finite temperature in reciprocal space can be represented by

$$H(T) = H_0 + H_B - JZN^{-1} \sum_{k,k',q} a_{k-q}^+ a_{k'+q}^+ a_{k'} a_k \Big(\gamma_{k-k'-q} - \frac{\gamma_{k-q}}{2} - \frac{\gamma_{k'}}{2} \Big). \tag{23}$$

There is no analytical solution for the four magnon operators, so it is necessary to decompose the products of four magnon operators. Wick's theorem, an algebraic strategy, states that the product of operators is equal to the sum of all possible pairs of operators, and allows one to handle the reduction problem quite easily. Here we adopt Wick's theorem to decouple the four-magnon operators to two-magnon order [68]:

$$a_{k-q}^+ a_{k'+q}^+ a_{k'} a_k = (a_{k-q}^+ a_{k'+q}^+)(a_{k'} a_k) + (a_{k-q}^+ a_{k'})(a_{k'+q}^+ a_k) + (a_{k-q}^+ a_k)(a_{k'+q}^+ a_{k'}). \tag{24}$$

Meanwhile, the low order Taylor approximation is used to simplify the Hamiltonian:

$$(a_{k-q}^+ a_{k'})(a_{k'+q}^+ a_k) = [\langle a_{k-q}^+ a_{k'} \rangle + (a_{k-q}^+ a_{k'} - \langle a_{k-q}^+ a_{k'} \rangle)][\langle a_{k'+q}^+ a_k \rangle + (a_{k'+q}^+ a_k - \langle a_{k'+q}^+ a_k \rangle)]. \tag{25}$$

Finally, the Hamiltonian at finite temperature can be written as

$$\begin{aligned} H(T) = H_0 + H_B + E_1 + JZN^{-1} \sum_{k,k',q} (&\langle a_{k-q}^+ a_k \rangle a_{k'+q}^+ a_{k'} + \langle a_{k'+q}^+ a_{k'} \rangle a_{k-q}^+ a_k + \langle a_{k-q}^+ a_{k'} \rangle a_{k'+q}^+ a_k \\ &+ \langle a_{k'+q}^+ a_k \rangle a_{k-q}^+ a_{k'} \Big(\frac{\gamma_{k-q}}{2} + \frac{\gamma_{k'}}{2} - 2\gamma_{k-k'-q} \Big), \end{aligned} \tag{26}$$

with $\sum_{k'} \gamma_{k-k'} = \gamma_k \sum_{k'} \gamma_{k'}$. E_1 is the static energy difference from the ground state. Consequently, the magnon dispersion at finite temperature can be described as

$$\hbar\omega_k^{\pm}(T) = E_{\mathrm{SI}}^{\pm} + E_{\mathrm{DI}}^{\pm}(T) + 2g\mu_B B = JZS_0(1 \pm \gamma_k) + JZS_0(1 \pm \gamma_k)\beta(T) + 2g\mu_B B, \tag{27}$$

with

$$\beta(T) = -\frac{1}{NS_0} \sum_{k'} (1 - \gamma_{k'}) \langle a_k^+ a_{k'} \rangle_T. \tag{28}$$

$E_{\mathrm{DI}}^{\pm}$ represents the magnon energy from "dynamical interaction," which is caused by the variety in magnon population induced by finite temperature [69]. The dynamical interaction is quite different from the nonlinear response used to describe magnon-phonon interaction [70]. It is obvious that the value of dynamical energy $E_{\mathrm{DI}}^{\pm}$ is proportional to the static exchange energy $E_{\mathrm{SI}}^{\pm}$ with a parameter β (T). β (T) can be called the "dynamical constant," and is plotted in Fig. 1 as a function of temperature. The increase in the absolute value of dynamical constant with temperature reveals the strengthening of dynamical interaction, which can be measured by neutron scattering [69]. In the present work, the magnon energy contributed by dynamical interaction is calculated by a self-consistent procedure.

C. Computational details

In this paper, we used the experimental lattice constants ($a = b = 6.83$ Å) [71], and the geometrical structure is relaxed by the Vienna *ab initio simulation* package (VASP) [72] using 500 eV cutoff energy. Due to the d-orbit electrons around the Cr atom, the generalized gradient approximation (GGA) with Hubbard "U" should be used as the exchange-correlation function [73]. Gong *et al.* [8] and Kang *et al.* [74] explored the influence of U on the electronic and magnetic properties of CGT monolayer and bulk. Kang *et al.* found that the CGT monolayer behaves as a semiconductor with a finite gap when $U = 0$, while calculation using $U = 3$ eV predicts a semimetallic state [74]. Gong *et al.* found that for $U < 0.2$ eV, the bulk CGT becomes in-plane anisotropic; for $U > 1.7$ eV the interlayer coupling becomes antiferromagnetic [8], which is contrary to the experimental results. Therefore, they suggest the value of U for CGT should be within the range from 0.2 to 1.7 eV, and we chose $U = 1$ eV as used in previous works in the literature [31,50]. For the CGT monolayer, a vacuum space of 16 Å is set along the out-of-plane direction to suppress the possible interaction between the atomic plane and its neighboring image. The convergence for the energy difference of self-consistent iterations and the Hellmann-Feynman force were 10^{-8} eV and 0.001 eV/Å, respectively. A k-point mesh of $5 \times 5 \times 1$ was used for structural relaxation, while a $9 \times 9 \times 1$ mesh was used for

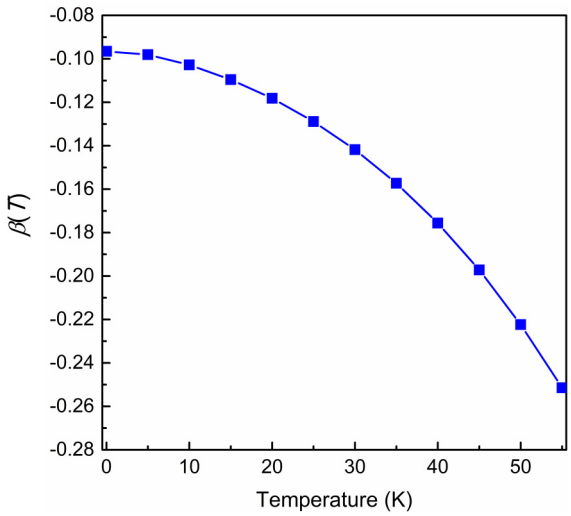

FIG. 1. The temperature dependence of dynamical constant $\beta(T)$.

self-consistent calculation to obtain the energy of the CGT unit cell under different magnetic configurations. Besides, the phonon spectrum and phonon density of state (PDOS) are calculated with a 23 × 23 × 1 mesh by the PHONOPY code.

III. RESULTS AND DISCUSSION

A. Spin-wave spectrum at finite temperature

The geometric structure and the path in the Brillouin zone of the CGT monolayer are shown in Fig. 2. It was reported that Te atoms play a fundamental role in stabilizing the ferromagnetism of monolayer CGT through the superexchange interaction between Te-Cr-Te bonds [75,76], although they are nonmagnetic. As shown in Table I, the optimized lattice constants ($a = b =$ 6.83 Å) agree well with previous reports [71]. The bond length of Cr-Te in the optimized CGT monolayer is 2.77 Å, which is much shorter than the distance (3.94 Å) between two Cr atoms in a unit cell. The phonon spectrum and PDOS of the optimized structure are presented in Fig. 3. It is obvious that there is no imaginary frequency at the Gamma point indicating the kinetic stability of our optimized structure. In detail, the phonon vibration with low frequency is mainly contributed by the Te atom whose mass is much larger than the Cr and Ge atoms. To determine the ground state, the energies of the CGT monolayer with ferromagnetic (FM) and antiferromagnetic (AFM) configurations are calculated as −48.407 and −48.345 eV. The diagram of ferromagnetic (FM) and antiferromagnetic (AFM) configuration is shown in Fig. 4, where the red and green arrows represent spin up and spin down, respectively.

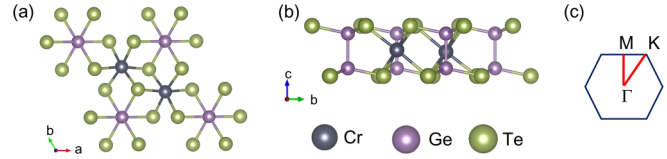

FIG. 2. (a) Top view and (b) side view of $Cr_2Ge_2Te_6$ (CGT) monolayer, and the irreducible Brillouin zone of CGT monolayer (c). The Cr, Ge, and Te atoms in (a), (b) are denoted in gray, purple, and dark green colors, respectively.

For FM configuration, the total energy of CGT unit cell can be written as

$$E_{\mathrm{FM}} = E_{\mathrm{N}} - JZS_0^2, \tag{29}$$

while that for antiferromagnetic configuration should be written as

$$E_{\mathrm{AFM}} = E_{\mathrm{N}} + JZS_0^2. \tag{30}$$

E_{N} is the energy of the CGT monolayer when magnetism is out of consideration, and Z is the coordination number for the nearest-neighboring exchange interaction. The magnetic moment of the Cr atom is obtained as 3.14 μ_B by VASP, which is very close to the ideal value (3 μ_B). So, we set S_0 as $\frac{3}{2}$ for Cr^{3+} ion. Then, the nearest-neighboring exchange constant can be calculated by

$$J = (E_{AFM} - E_{FM})/(2ZS_0^2). \tag{31}$$

The ground state of the CGT monolayer can be determined through comparing E_{FM} to E_{AFM}. If E_{FM} is lower than E_{AFM} (a positive exchange constant), the ground state is ferromagnetic. On the opposite side, the negative exchange constant reveals the antiferromagnetism ground state. At zero temperature, the nearest-neighbor exchange constant in the CGT monolayer is 4.557 meV, revealing the FM ground state. In the following section, we would use the exchange constant J at zero temperature to calculate the magnon dispersion and investigate the MMI, following the previous studies [77,78] because the temperature dependence of J is negligible. Moreover, we also predicted the Curie temperature as 53 K of the CGT monolayer using mean-field theory by [31,65]

$$T_{\mathrm{C}} = \frac{ZJ}{3k_B}, \tag{32}$$

which agrees well with the Curie temperature T_{c} of 60 K in previous theoretical and experimental reports [76,79,80]. The Curie temperature and other magnetic properties of monolayer CGT are summarized in Table II. Here, we focus on

TABLE I. Lattice constant, length of Cr-Te bond, the bond angle of Cr-Te-Cr, and distance of the nearest exchange coupling for $Cr_2Ge_2Te_6$ monolayer.

Lattice parameter (Å)	Bond length of Cr-Te (Å)	Bond angle of Cr-Te-Cr (deg)	Distance for nearest coupling (Å)
6.83	2.77	84.43	3.94

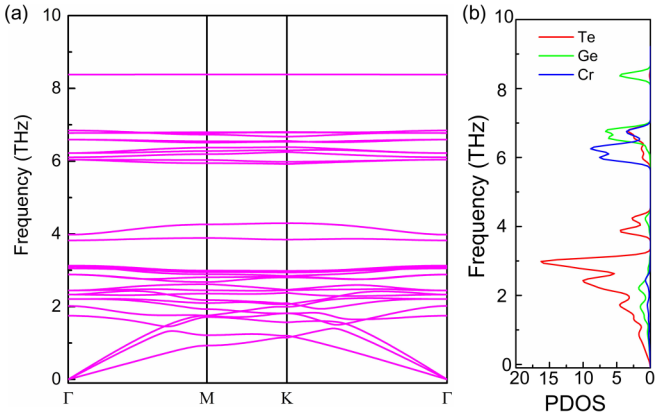

FIG. 3. (a) Phonon spectrum and (b) phonon density of state (PDOS) of CGT monolayer.

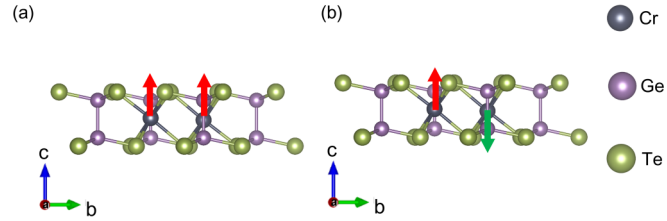

FIG. 4. The diagram of ferromagnetic (FM) and antiferromagnetic (AFM) configurations in CGT monolayer. The red arrow represents spin up, while the green arrow represents spin down.

the MMI at the finite temperature below 60 K. The magnon dispersions of the CGT monolayer calculated through Eq. (30) at temperatures of 0, 15, 30, and 45 K are represented by black, red, blue, and green spheres in Fig. 5(a). It is obvious that the acoustic branch of the spin-wave spectrum shows zero frequencies at the Γ point, different from the case in CrI_3 [81]. This is because the magnetic anisotropy is ignored in the Heisenberg Hamiltonian of the CGT monolayer, while the magnetic anisotropy of CrI_3 is comparable to its exchange interaction and cannot be neglected [29,33]. In addition, an external magnetic field of 0.1 T along the c axis is taken into consideration in the spin-wave spectrum because of the Zeeman energy in the Heisenberg Hamiltonian. It can be found that the magnon frequency at finite temperature is consistent globally with the zero temperature spectra except for a slight redshift. The temperature induced redshift in magnon dispersion at finite temperature should be ascribed to the correction energy E_{DI} caused by the dynamical interaction.

The correction energies E_{DI} caused by the dynamical interaction for optical and acoustic magnons are presented in Figs. 5(b) and 5(c). It should be noted that the range of the Y axis in Fig. 5(b) is 0.2 to -1.4 meV which is about 25 times smaller than that in Fig. 5(a), so that the acoustic mode in Fig. 5(b) looks changed more obviously with temperature. To observe the relationship between E_{SI} and E_{DI}, we sampled the wave vectors from the center (Γ) to the boundary (M) of the Brillouin zone. All of the correction energies E_{DI} at $k = 1.03 \times 10^6$ (0.02), 1.03×10^7 (0.2), 2.06×10^7 (0.4), 3.09×10^7 (0.6), 4.12×10^7 (0.8), and $5.15 \times 10^7\ \mathrm{cm}^{-1}$ (1.0 π/a) are negative revealing the influence of dynamical interaction on the spin-wave spectrum is to reduce the magnon frequency. The decrease in an optical magnon is more pronounced than that in an acoustic magnon, because the correction energy E_{DI} is proportional to the static magnon energy E_{SI} as shown in Eq. (30). More importantly, the correction energies E_{DI} at all k points become more negative with the increase of temperature, which is consistent with previous theoretical study on EuO using Dyson-Maleev theory [69].

B. Magnon-magnon interaction and spin autocorrelation function

In this work, the MMI strength is investigated by calculating the spin autocorrelation functions $\langle S_k^+(t)S_{-k}^-(0)\rangle$, $\langle S_k^-(t)S_{-k}^+(0)\rangle$, and $\langle S_k^z(t)S_{-k}^-(0)\rangle$. These spin autocorrelation functions are supposed to dominate electric spin injection, chemical potential-driven transport, which is related to the spin Seebeck effect [78,82,83]. The solutions of the Heisenberg equation of motion, $i\hbar\frac{\partial a_k(a_k^+)}{\partial t} = \hbar\omega_k a_k(a_k^+)$, based on $H(T)$ for $a_k(t)$ and $a_k^+(t)$ are

$$a_k(t) = a_k(0)e^{-i\omega_k t}, \quad a_k^+(t) = a_k^+(0)e^{i\omega_k t}. \tag{33}$$

Due to the external magnetic field along the c axis, we would put particular emphasis on the spin autocorrelation function $\langle S_k^z(t)S_{-k}^z(0)\rangle$. In the reciprocal space, S_k^z can be represented as

$$S_k^z = N^{-\frac{1}{2}}\sum_l e^{-i\mathbf{k}\cdot\mathbf{r}_l}S_l^z = N^{\frac{1}{2}}S_0\delta_{k,0} - N^{-\frac{1}{2}}\sum_{k'} a_{k'}^+ a_{k'+k}. \tag{34}$$

TABLE II. Magnetic moment on Cr^{3+} ion, energies for in-plane and out-of-plane magnetization, magnetic anisotropy energy, and Curie temperature for $Cr_2Ge_2Te_6$ monolayer.

Magnetic moment (μ_B)	Energy for in-plane FM (eV)	Energy for out-of-plane FM (eV)	Magnetic anisotropy energy (meV)	Curie temperature (K)
3.14	–49.0513	–49.0510	–0.3	53

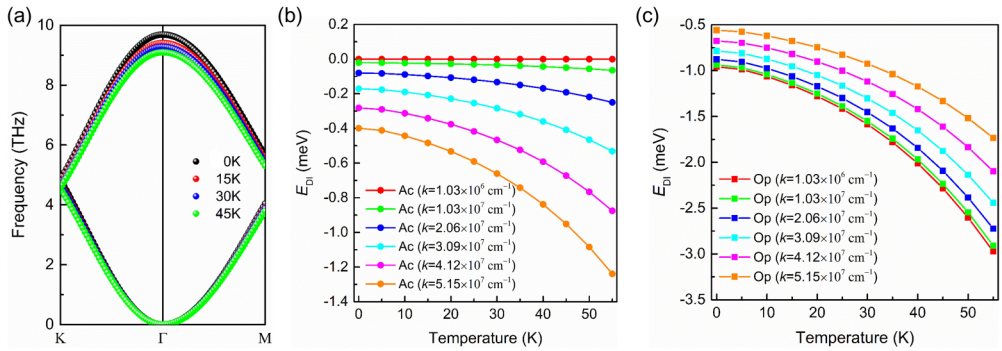

FIG. 5. Effects of temperature on spin-wave spectrums (a); the correction energies $E_{\rm DI}$ from dynamical interaction for acoustic (b) and optical (c) magnons in CGT monolayer at finite temperature. In (b), (c), wave vector $k = 1.03 \times 10^6$ (0.02), 1.03×10^7 (0.2), 2.06×10^7 (0.4), 3.09×10^7 (0.6), 4.12×10^7 (0.8), and 5.15×10^7 cm^{-1} ($1.0\,\pi/a$) are sampled along the path from center (Γ) to boundary (M) in the Brillouin zone.

Then $\langle S^z_k(t)S^z_{-k}(0)\rangle$ can be written as

$$\begin{aligned}\left\langle S^z_k(t)S^z_{-k}(0)\right\rangle &= \frac{\mathrm{Tr}\left(e^{-\theta H}\left\{\left[N^{\frac{1}{2}}S_0\delta_{k,0} - N^{-\frac{1}{2}}\sum_{k'} a^+_{k'}(t)a_{k'+k}(t)\right]\left[N^{\frac{1}{2}}S_0\delta_{-k,0} - N^{-\frac{1}{2}}\sum_{k''} a^+_{k''}(0)a_{k''-k}(0)\right]\right\}\right)}{\mathrm{Tr}(e^{-\theta H})} \\ &= \left\langle NS_0{}^2\delta_{k,0}\right\rangle - S_0\delta_{k,0}\left\langle\left[\sum_{k'} a^+_{k'}(t)a_{k'+k}(t) + \sum_{k''} a^+_{k''}(0)a_{k''-k}(0)\right]\right\rangle + N^{-1}\sum_{k',k''}\langle a^+_{k'}(t)a_{k'+k}(t)a^+_{k''}(0)a_{k''-k}(0)\rangle \\ &= NS_0{}^2\delta_{k,0} - 2S_0\delta_{k,0}\sum_{k'}\langle a^+_{k'}(0)a_{k'+k}(0)\rangle + N^{-1}\sum_{k'} e^{-i(\omega_{k'+k}-\omega_{k'})t}\left\langle a^+_{k'}(0)a_{k'+k}(0)a^+_{k'+k}(0)a_{k'}(0)\right\rangle. \end{aligned} \tag{35}$$

Here, we also employed Wick's theorem to decouple these four magnon operators [68], and it is

$$\left\langle S^z_k(t)S^z_{-k}(0)\right\rangle = \begin{cases} NS_0{}^2\delta_{k,0} - 2S_0\delta_{k,0}\sum_{k'}\langle n_{k'}\rangle + N^{-1}\sum_{k'}(2\langle n_{k'}\rangle^2 + \langle n_{k'}\rangle) & (k=0) \\ N^{-1}\sum_{k'} e^{-i(\omega_{k'+k}-\omega_{k'})t}\langle n_{k'}\rangle\langle n_{k'+k}+1\rangle & (k\neq 0) \end{cases}, \tag{36}$$

with $\langle n_k\rangle = \langle a^+_k a_k\rangle$. It is worth noting that $\langle n_k\rangle$ is mainly contributed by acoustic magnons with respect to optical magnons, because of the low population of the latter. The spin autocorrelation functions in the long-wavelength limit ($k = 5.15 \times 10^4$ cm^{-1} $= 0.001\ \pi/a$) at 55 and 5 K, and under external magnetic field B of 0.1 T are shown in Figs. 6(a) and 6(b), while that in the short-wavelength limit ($k = 5.15 \times 10^7$ cm^{-1} $= 1\,\pi/a$, with $T = 55$ K and $B = 5$ T) is presented in Fig. 6(c). As shown in Fig. 6(a), it is obvious that the spin autocorrelation function decays with time and gradually converges. It is noted that the spin autocorrelation function is used to investigate the decay of the magnon energy with time at a specific wave vector. When the amplitude of the spin autocorrelation function is zero, it reveals complete decoherence of magnons. In order to obtain the relaxation time $\tau_{\rm MM}$ governed by magnon-magnon interaction, an exponential decay function $[f(t) = A\exp(-t/\tau_{\rm MM})]$ was employed to fit the envelope of spin autocorrelation function, as plotted by the red solid line in Fig. 6. The relaxation time $\tau_{\rm MM}$ of the spin autocorrelation function can reflect the strength of MMI, and the shorter $\tau_{\rm MM}$ corresponds to a stronger MMI.

Comparing Figs. 6(a) with 6(b), there is a significant temperature dependence in the decay rate of spin autocorrelation function when temperature T decreases from 55 to 5 K. Comparing Figs. 6(a) with 6(c), it can be found that the increase of wave vector k from the long-wavelength limit to the short-wavelength limit causes substantial reduction in the relaxation time $\tau_{\rm MM}$. Besides, when the external magnetic field B increases from 0.1 to 5 T, the decay rate of spin autocorrelation function also increases. Figure 6(d) presents the spin autocorrelation function at $k = 5.15 \times 10^4$ cm^{-1} for $T = 55$ K and $B = 0.1$ T, where only the contribution of acoustic magnons is taken into consideration. Comparing Figs. 6(a) to 6(d), similar results [$\tau_{\rm MM} = 120\,\mu$s for Fig. 6(a) and $\tau_{\rm MM} = 146\,\mu$s for Fig. 6(d)] suggest the spin autocorrelation function is mainly raised from acoustic magnon-magnon interaction. Next, we systematically explore the dependence of the spin autocorrelation function and relaxation time $\tau_{\rm MM}$ on wave vector k, temperature T, and magnetic field B.

C. Magnon relaxation time

In Fig. 7 the wave vector dependence, the temperature dependence, and the frequency dependence of the relaxation time are presented. Firstly, we focus on the wave-vector dependence. Here, we extract the relaxation time $\tau_{\rm MM}$ based on the spin autocorrelation function throughout the whole wavelength regime, temperature is fixed at 30 K, and magnetic field is 0.1 T, as shown in Fig. 7(a). It is obvious that the relaxation time $\tau_{\rm MM}$ decreases monotonously with wave vector k. The energy of acoustic magnon at the boundary of the Brillouin zone is much higher than that at the zone center, and the

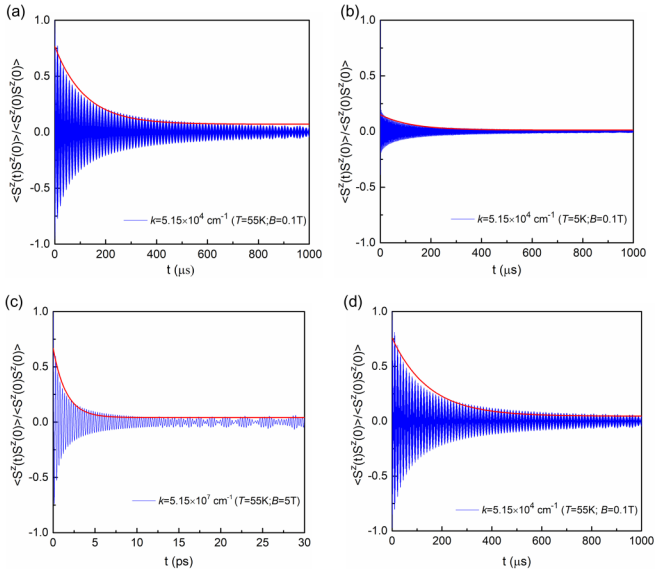

FIG. 6. (a) Autocorrelation function at $k = 5.15 \times 10^4\,\mathrm{cm}^{-1}$ at external magnetic field $B = 0.1\,\mathrm{T}$ and temperature $T = 55\,\mathrm{K}$. (b) Autocorrelation function at $k = 5.15 \times 10^4\,\mathrm{cm}^{-1}$ at external magnetic field $B = 0.1\,\mathrm{T}$ and temperature $T = 5\,\mathrm{K}$. (c) Autocorrelation function at $k = 5.15 \times 10^7\,\mathrm{cm}^{-1}$ at $T = 55\,\mathrm{K}$ and $B = 5\,\mathrm{T}$. (d) The spin autocorrelation function only contributed by acoustic magnons. In (d), $k = 5.15 \times 10^4\,\mathrm{cm}^{-1}$, $T = 55\,\mathrm{K}$, and $B = 0.1\mathrm{T}$. The red solid lines represent the results fitted by exponential decay functions.

higher magnon energy leads to a faster decay rate of spin autocorrelation function.

The temperature dependence of relaxation time τ_{MM} for magnons in the long-wavelength limit ($k = 5.15 \times 10^4\,\mathrm{cm}^{-1} = 0.001\ \pi/a$) and at the boundary of the Brillouin zone ($k = 5.15 \times 10^7\,\mathrm{cm}^{-1} = 1\,\pi/a$) is presented in Fig. 7(b). It is interesting that the relaxation times τ_{MM} in the long-wavelength limit and the short-wavelength limit show completely opposite temperature dependence. In the long-wavelength limit, the relaxation time τ_{MM} increases with temperature, while it shows a reduction with temperature increasing at the boundary of the Brillouin zone. It can be obtained from Eq. (36) that the decay rate of spin autocorrelation function depends on the magnon frequency. However, the magnon frequency decreases with temperature due to the dynamical interaction, as shown in Fig. 5. Therefore, the decay rate of spin autocorrelation function reduces with temperature, which leads to the increase in relaxation time τ_{MM} for long-wavelength magnons. At the boundary of Brillouin zone, relaxation time τ_{MM} decreases with temperature due to the strong anharmonic behavior. In Fig. 7(c), we present the frequency dependence of relaxation time τ_{MM} under magnetic field $B = 1\,\mathrm{T}$ at different temperatures ($T = 10$–$50\,\mathrm{K}$). It is obvious that the relaxation time τ_{MM} at different temperatures show similar frequency dependence. Meantime, an anharmonic behavior can be observed.

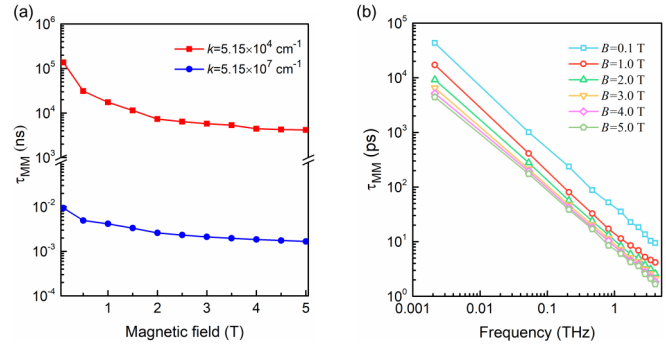

FIG. 8. (a) The magnetic field dependence of τ_{MM} at $T = 30\,\mathrm{K}$. (b) The frequency dependence of τ_{MM} at $T = 30\,\mathrm{K}$ when magnetic field varies from 0.1 to 5 T. In (b), the τ_{MM} versus frequency curves are shown in log-log scale.

The dependence of relaxation time τ_{MM} on the strength of magnetic field at $k = 5.15 \times 10^4\,\mathrm{cm}^{-1}$ and $k = 5.15 \times 10^7\,\mathrm{cm}^{-1}$ at $T = 30\,\mathrm{K}$ are presented in Fig. 8(a). It is found that the relaxation time in both long-wavelength and short-wavelength limits decreases with the enhancement of magnetic field, which is opposite of temperature dependence. Such an enhancement of the magnetic field increases the magnon frequency ω_k, resulting in the rapid decay of spin autocorrelation function. These opposite impacts between temperature and magnetic field can also be observed in Fig. 9, which shows the normalized magnetic moment per Cr^{3+} ion

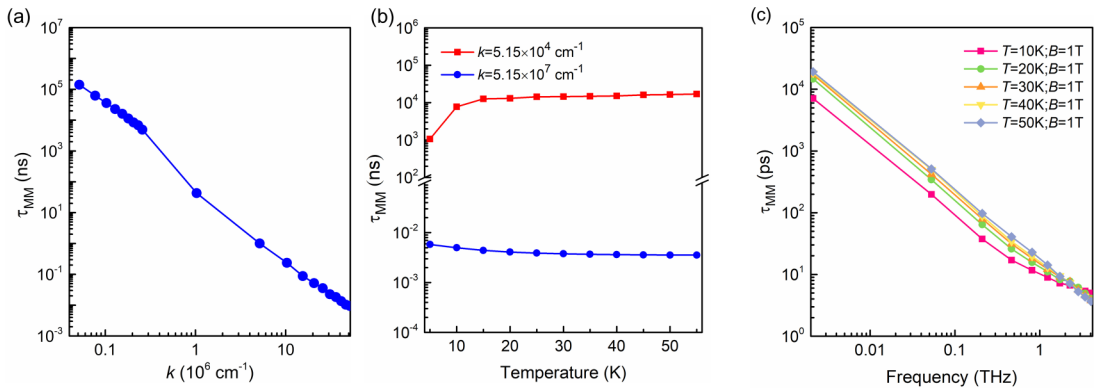

FIG. 7. (a) The wave-vector dependence of relaxation time τ_{MM} governed by magnon-magnon interaction at $T = 30\,\mathrm{K}$ and $B = 0.1\,\mathrm{T}$. It is plotted in log-log scale. (b) The temperature dependence of τ_{MM} at $k = 5.15 \times 10^4\,\mathrm{cm}^{-1}$ and $k = 5.15 \times 10^7\mathrm{cm}^{-1}$. Here $B = 1.0\,\mathrm{T}$. (c) τ_{MM} as a function of acoustic magnon frequency. Here $B = 1.0\,\mathrm{T}$, and temperature changes from 10 to 50 K.

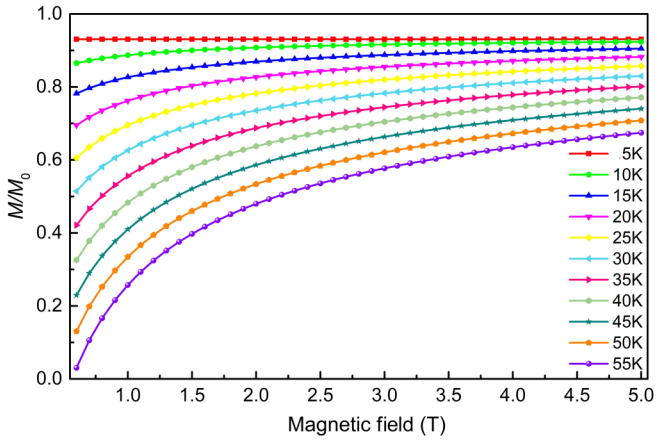

FIG. 9. The magnetic moment per Cr^{3+} ion normalized to M_0 ($M_0 = 3\,\mu_B$) versus magnetic field. In this figure, the temperature changes from 5 to 55 K.

at different temperature and magnetic field. The magnetic moment M per Cr^{3+} ion is calculated by [84]:

$$M(B,T) = g\mu_B \sum_l (S_0 - \langle a_l^+ a_l \rangle_{B,T}) = M_0 \left(1 - \frac{1}{NS_0} \sum_k \langle a_k^+ a_k \rangle_{B,T}\right), \quad (37)$$

where $M_0 = g\mu_B S_0 = 3\mu_B$ is the magnetic moment of Cr^{3+} at zero temperature. The dependence of normalized magnetic moment to M_0 on magnetic field B at different temperatures is shown in Fig. 9. It is obvious that the magnetic moment grows with the enhancement of the magnetic field and tends to a specific value, while it decreases close to zero with the increase of temperature. These results reveal the magnon density $\langle a_k^+ a_k \rangle$ increases with temperature but decreases with the enhancement of magnetic field [85], which is in agreement with results in Figs. 7 and 8. Figure 8(b) presents τ_{MM} as a function of frequency under different magnetic field. Overall, τ_{MM} decreases with frequency increases, independent of the strength of the magnetic field.

IV. CONCLUSIONS

In summary, we established the Heisenberg Hamiltonian model for ferromagnetic 2D materials at finite temperature by taking the dynamical interaction into consideration. Based on this Hamiltonian model, it is found the increase of temperature results in a non-negligible reduction in the spin-wave spectrum, especially the optical branch. Furthermore, the relaxation time τ_{MM} governed by magnon-magnon interaction is also calculated based on decay of spin autocorrelation function. We find the relaxation time τ_{MM} increases with temperature but decreases with wave vector and magnetic field, because of the different magnon energy trends. All these results presented in our work are helpful for the utilization and manipulation of ferromagnetic 2D materials for applications in spintronic devices.

ACKNOWLEDGMENTS

We gratefully acknowledge the financial support from the Graduate School of Xidian University and the China Scholarship Council (Grant No. 201906960032), and the use of computing resources at the Agency for Science, Technology and Research (A*STAR) Computational Resource Centre, Singapore.

[1] A. J. Mannix, B. Kiraly, M. C. Hersam, and N. P. Guisinger, Synthesis and chemistry of elemental 2D materials, Nat. Rev. Chem. **1**, 1 (2017).

[2] L. Tao, E. Cinquanta, D. Chiappe, C. Grazianetti, M. Fanciulli, M. Dubey, A. Molle, and D. Akinwande, Silicene field-effect transistors operating at room temperature, Nat. Nanotechnol. **10**, 227 (2015).

[3] K. Novoselov, A. Mishchenko, A. Carvalho, and A. C. Neto, 2D materials and van der Waals heterostructures, Science **353**, aac9439 (2016).

[4] S. Manzeli, D. Ovchinnikov, D. Pasquier, O. V. Yazyev, and A. Kis, 2D transition metal dichalcogenides, Nat. Rev. Mater. **2**, 17033 (2017).

[5] M. Ashton, J. Paul, S. B. Sinnott, and R. G. Hennig, Topology-Scaling Identification of Layered Solids and Stable Exfoliated 2D Materials, Phys. Rev. Lett. **118**, 106101 (2017).

[6] N. Mounet, M. Gibertini, P. Schwaller, D. Campi, A. Merkys, A. Marrazzo, T. Sohier, I. E. Castelli, A. Cepellotti, G. Pizzi, and N. Marzari, Two-dimensional materials from high-throughput computational exfoliation of experimentally known compounds, Nat. Nanotechnol. **13**, 246 (2018).

[7] M. Gibertini, M. Koperski, A. Morpurgo, and K. Novoselov, Magnetic 2D materials and heterostructures, Nat. Nanotechnol. **14**, 408 (2019).

[8] C. Gong, L. Li, Z. Li, H. Ji, A. Stern, Y. Xia, T. Cao, W. Bao, C. Wang, Y. Wang, Z. Q. Qiu, R. J. Cava, S. G. Louie, J. Xia, and X. Zhang, Discovery of intrinsic ferromagnetism in two-dimensional van der Waals crystals, Nature **546**, 265 (2017).

[9] B. Huang, G. Clark, D. R. Klein, D. MacNeill, E. Navarro-Moratalla, K. L. Seyler, N. Wilson, M. A. McGuire, D. H. Cobden, D. Xiao, W. Yao, P. Jarillo-Herrero, and X. Xu, Electrical control of 2D magnetism in bilayer CrI3, Nat. Nanotechnol. **13**, 544 (2018).

[10] A. F. May, D. Ovchinnikov, Q. Zheng, R. Hermann, S. Calder, B. Huang, Z. Fei, Y. Liu, X. Xu, and M. A. McGuire, Ferromagnetism near room temperature in the cleavable van der Waals crystal Fe_5GeTe_2, ACS Nano **13**, 4436 (2019).

[11] Z. Fei, B. Huang, P. Malinowski, W. Wang, T. Song, J. Sanchez, W. Yao, D. Xiao, X. Zhu, A. F. May, W. Wu, D. H. Cobden, J.-H. Chu, and X. Xu, Two-dimensional itinerant ferromagnetism in atomically thin Fe_5GeTe_2, Nat. Mater. **17**, 778 (2018).

[12] Y. Shiomi, R. Takashima, and E. Saitoh, Experimental evidence consistent with a magnon Nernst effect in the antiferromagnetic insulator $MnPS_3$, Phys. Rev. B **96**, 134425 (2017).

[13] G. Long, H. Henck, M. Gibertini, D. Dumcenco, Z. Wang, T. Taniguchi, K. Watanabe, E. Giannini, and A. F. Morpurgo, Persistence of magnetism in atomically thin $MnPS_3$ crystals, Nano Lett. **20**, 2452 (2020).

[14] S. Kim, J. Lee, G. Jin, M.-H. Jo, C. Lee, and S. Ryu, Crossover between photochemical and photothermal oxidations of atomically thin magnetic semiconductor $CrPS_4$, Nano Lett. **19**, 4043 (2019).

[15] A. K. Budniak, N. A. Killilea, S. J. Zelewski, M. Sytnyk, Y. Kauffmann, Y. Amouyal, R. Kudrawiec, W. Heiss, and E. Lifshitz, Exfoliated $CrPS_4$ with promising photoconductivity, Small **16**, 1905924 (2020).

[16] A. McCreary, J. R. Simpson, T. T. Mai, R. D. McMichael, J. E. Douglas, N. Butch, C. Dennis, R. V. Aguilar, and A. R. H. Walker, Quasi-two-dimensional magnon identification in antiferromagnetic $FePS_3$ via magneto-Raman spectroscopy, Phys. Rev. B **101**, 064416 (2020).

[17] M. Shentcis, A. K. Budniak, X. Shi, R. Dahan, Y. Kurman, M. Kalina, H. Herzig Sheinfux, M. Blei, M. K. Svendsen, Y. Amouyal, S. Tongay, K. S. Thygesen, F. H. L. Koppens, E. Lifshitz, F. J. García de Abajo, L. J. Wong, and I. Kaminer, Tunable free-electron x-ray radiation from van der Waals materials, Nat. Photonics **14**, 686 (2020).

[18] W. Yang, A. L. Coughlin, L. Webster, G. Ye, K. Lopez, H. A. Fertig, R. He, J.-A. Yan, and S. Zhang, Highly tunable Raman scattering and transport in layered magnetic Cr_2S_3 nanoplates grown by sulfurization, 2D Mater. **6**, 035029 (2019).

[19] F. Cui, X. Zhao, J. Xu, B. Tang, Q. Shang, J. Shi, Y. Huan, J. Liao, Q. Chen, Y. Hou, Q. Zhang, S. J. Pennycook, and Y. Zhang, Controlled growth and thickness-dependent conduction-type transition of 2D ferrimagnetic Cr_2S_3 semiconductors, Adv. Mater. **32**, 1905896 (2020).

[20] S. Zhang, R. Xu, W. Duan, and X. Zou, Intrinsic half-metallicity in 2D ternary chalcogenides with high critical temperature and controllable magnetization direction, Adv. Funct. Mater. **29**, 1808380 (2019).

[21] Q. Wu, Y. Zhang, Q. Zhou, J. Wang, and X. C. Zeng, Transition-metal dihydride monolayers: A new family of two-dimensional ferromagnetic materials with intrinsic room-temperature half-metallicity, J. Phys. Chem. Lett. **9**, 4260 (2018).

[22] T. Zhang, Y. Wang, H. Li, F. Zhong, J. Shi, M. Wu, Z. Sun, W. Shen, B. Wei, W. Hu, X. Liu, L. Huang, C. Hu, Z. Wang, C. Jiang, S. Yang, Q.-m. Zhang, and Z. Qu, Magnetism and optical anisotropy in van der Waals antiferromagnetic insulator CrOCl, ACS Nano **13**, 11353 (2019).

[23] N. Miao, B. Xu, L. Zhu, J. Zhou, and Z. Sun, 2D intrinsic ferromagnets from van der Waals antiferromagnets, J. Am. Chem. Soc. **140**, 2417 (2018).

[24] A. Bandyopadhyay, N. C. Frey, D. Jariwala, and V. B. Shenoy, Engineering magnetic phases in two-dimensional non-van der Waals transition-metal oxides, Nano Lett. **19**, 7793 (2019).

[25] J. He, G. Ding, C. Zhong, S. Li, D. Li, and G. Zhang, Cr_2TiC_2-based double MXenes: Novel 2D bipolar antiferromagnetic semiconductor with gate-controllable spin orientation toward antiferromagnetic spintronics, Nanoscale **11**, 356 (2019).

[26] N. C. Frey, A. Bandyopadhyay, H. Kumar, B. Anasori, Y. Gogotsi, and V. B. Shenoy, Surface-engineered MXenes: Electric field control of magnetism and enhanced magnetic anisotropy, ACS Nano **13**, 2831 (2019).

[27] L. Webster and J.-A. Yan, Strain-tunable magnetic anisotropy in monolayer $CrCl_3$, $CrBr_3$, and CrI_3, Phys. Rev. B **98**, 144411 (2018).

[28] J. A. Sears, L. E. Chern, S. Kim, P. J. Bereciartua, S. Francoual, Y. B. Kim, and Y.-J. Kim, Ferromagnetic Kitaev interaction and the origin of large magnetic anisotropy in α-$RuCl_3$, Nat. Phys. **16**, 837 (2020).

[29] C. Xu, J. Feng, H. Xiang, and L. Bellaiche, Interplay between Kitaev interaction and single ion anisotropy in ferromagnetic CrI_3 and $CrGeTe_3$ monolayers, npj Comput Mater. **4**, 1 (2018).

[30] J. L. Lado and J. Fernández-Rossier, On the origin of magnetic anisotropy in two dimensional CrI_3, 2D Mater. **4**, 035002 (2017).

[31] Y. Fang, S. Wu, Z.-Z. Zhu, and G.-Y. Guo, Large magneto-optical effects and magnetic anisotropy energy in two-dimensional $Cr_2Ge_2Te_6$, Phys. Rev. B **98**, 125416 (2018).

[32] N. D. Mermin and H. Wagner, Absence of Ferromagnetism or Antiferromagnetism in One-or Two-Dimensional Isotropic Heisenberg Models, Phys. Rev. Lett. **17**, 1133 (1966).

[33] I. Lee, F. G. Utermohlen, D. Weber, K. Hwang, C. Zhang, J. van Tol, J. E. Goldberger, N. Trivedi, and P. C. Hammel, Fundamental Spin Interactions Underlying the Magnetic Anisotropy in the Kitaev Ferromagnet CrI_3, Phys. Rev. Lett. **124**, 017201 (2020).

[34] H. Kumar, N. C. Frey, L. Dong, B. Anasori, Y. Gogotsi, and V. B. Shenoy, Tunable magnetism and transport properties in nitride MXenes, ACS Nano **11**, 7648 (2017).

[35] N. C. Frey, H. Kumar, B. Anasori, Y. Gogotsi, and V. B. Shenoy, Tuning noncollinear spin structure and anisotropy in ferromagnetic nitride MXenes, ACS Nano **12**, 6319 (2018).

[36] M. Rassekh, J. He, S. F. Shayesteh, and J. J. Palacios, Remarkably enhanced Curie temperature in monolayer CrI_3 by hydrogen and oxygen adsorption: A first-principles calculations, Comput. Mater. Sci. **183**, 109820 (2020).

[37] Z. Wang, T. Zhang, M. Ding, B. Dong, Y. Li, M. Chen, X. Li, J. Huang, H. Wang, X. Zhao, Y. Li, D. Li, C. Jia, L. Sun, H. Guo, Y. Ye, D. Sun, Y. Chen, T. Yang, J. Zhang, S. Ono, Z. Han, and Z. Zhang, Electric-field control of magnetism in a few-layered van der Waals ferromagnetic semiconductor, Nat. Nanotechnol. **13**, 554 (2018).

[38] K. Wang, T. Hu, F. Jia, G. Zhao, Y. Liu, I. V. Solovyev, A. P. Pyatakov, A. K. Zvezdin, and W. Ren, Magnetic and electronic properties of $Cr_2Ge_2Te_6$ monolayer by strain and electric-field engineering, Appl. Phys. Lett. **114**, 092405 (2019).

[39] X.-J. Dong, J.-Y. You, B. Gu, and G. Su, Strain-Induced Room-Temperature Ferromagnetic Semiconductors with Large Anomalous Hall Conductivity in Two-Dimensional $Cr_2Ge_2Se_6$, Phys. Rev. Appl. **12**, 014020 (2019).

[40] M. Wu, Z. Li, T. Cao, and S. G. Louie, Physical origin of giant excitonic and magneto-optical responses in two-dimensional ferromagnetic insulators, Nat. Commun. **10**, 1 (2019).

[41] J.-F. Dayen, S. J. Ray, O. Karis, I. J. Vera-Marun, and M. V. Kamalakar, Two-dimensional van der Waals spinterfaces and magnetic-interfaces, Appl. Phys. Rev. **7**, 011303 (2020).

[42] J. Li, Y. Li, S. Du, Z. Wang, B.-L. Gu, S.-C. Zhang, K. He, W. Duan, and Y. Xu, Intrinsic magnetic topological insulators in van der Waals layered $MnBi_2Te_4$-family materials, Sci. Adv. **5**, eaaw5685 (2019).

[43] M. Lohmann, T. Su, B. Niu, Y. Hou, M. Alghamdi, M. Aldosary, W. Xing, J. Zhong, S. Jia, and W. Han, Probing magnetism in insulating $Cr_2Ge_2Te_6$ by induced anomalous Hall effect in Pt, Nano Lett. **19**, 2397 (2019).

[44] M.-G. Han, J. A. Garlow, Y. Liu, H. Zhang, J. Li, D. DiMarzio, M. W. Knight, C. Petrovic, D. Jariwala, and Y. Zhu, Topological magnetic-spin textures in two-dimensional van der Waals $Cr_2Ge_2Te_6$, Nano Lett. **19**, 7859 (2019).

[45] R. Samajdar, M. S. Scheurer, S. Chatterjee, H. Guo, C. Xu, and S. Sachdev, Enhanced thermal Hall effect in the square-lattice Néel state, Nat. Phys. **15**, 1290 (2019).

[46] S. Park, N. Nagaosa, and B.-J. Yang, Thermal Hall effect, spin Nernst effect, and spin density induced by a thermal gradient in collinear ferrimagnets from magnon–phonon interaction, Nano Lett. **20**, 2741 (2020).

[47] L. Du, J. Tang, Y. Zhao, X. Li, R. Yang, X. Hu, X. Bai, X. Wang, K. Watanabe, and T. Taniguchi, Lattice dynamics, phonon chirality, and spin–phonon coupling in 2D itinerant ferromagnet Fe_5GeTe_2, Adv. Funct. Mater. **29**, 1904734 (2019).

[48] J. E. F. S. Rodrigues, W. S. Rosa, M. M. Ferrer, T. R. Cunha, M. J. Moreno Zapata, J. R. Sambrano, J. L. Martínez, P. S. Pizani, J. A. Alonso, A. C. Hernandes, and R. V. Gonçalves, Spin-phonon coupling in uniaxial anisotropic spin-glass based on Fe_2TiO_5 pseudobrookite, J. Alloys Compd. **799**, 563 (2019).

[49] L. Webster, L. Liang, and J.-A. Yan, Distinct spin–lattice and spin–phonon interactions in monolayer magnetic CrI_3, Phys. Chem. Chem. Phys. **20**, 23546 (2018).

[50] B. Zhang, Y. Hou, Z. Wang, and R. Wu, First-principles studies of spin-phonon coupling in monolayer $Cr_2Ge_2Te_6$, Phys. Rev. B **100**, 224427 (2019).

[51] L.-W. Wang, L.-S. Xie, P.-X. Xu, and K. Xia, First-principles study of magnon-phonon interactions in gadolinium iron garnet, Phys. Rev. B **101**, 165137 (2020).

[52] K. Wang, J. He, M. Zhang, H. Wang, and G. Zhang, Magnon–phonon interaction in antiferromagnetic two-dimensional MXenes, Nanotechnology **31**, 435705 (2020).

[53] P. Jiang, C. Wang, D. Chen, Z. Zhong, Z. Yuan, Z.-Y. Lu, and W. Ji, Stacking tunable interlayer magnetism in bilayer CrI_3, Phys. Rev. B **99**, 144401 (2019).

[54] K. Guo, B. Deng, Z. Liu, C. Gao, Z. Shi, L. Bi, L. Zhang, H. Lu, P. Zhou, L. Zhang, Y. Cheng, and B. Peng, Layer dependence of stacking order in nonencapsulated few-layer CrI_3, Sci. China Mater. **63**, 413 (2020).

[55] S. Jiang, L. Li, Z. Wang, K. F. Mak, and J. Shan, Controlling magnetism in 2D CrI_3 by electrostatic doping, Nat. Nanotechnol. **13**, 549 (2018).

[56] H. Tsai, T. Higo, K. Kondou, T. Nomoto, A. Sakai, A. Kobayashi, T. Nakano, K. Yakushiji, R. Arita, S. Miwa, Y. Otani, and S. Nakatsuji, Electrical manipulation of a topological antiferromagnetic state, Nature **580**, 608 (2020).

[57] T. Song, Z. Fei, M. Yankowitz, Z. Lin, Q. Jiang, K. Hwangbo, Q. Zhang, B. Sun, T. Taniguchi, K. Watanabe, M. A. McGuire, D. Graf, T. Cao, J.-H. Chu, D. H. Cobden, C. R. Dean, D. Xiao, and X. Xu, Switching 2D magnetic states via pressure tuning of layer stacking, Nat. Mater. **18**, 1298 (2019).

[58] T. Li, S. Jiang, N. Sivadas, Z. Wang, Y. Xu, D. Weber, J. E. Goldberger, K. Watanabe, T. Taniguchi, C. J. Fennie, K. Fai Mak, and J. Shan, Pressure-controlled interlayer magnetism in atomically thin CrI_3, Nat. Mater. **18**, 1303 (2019).

[59] C. P. Hofmann, Low-temperature properties of two-dimensional ideal ferromagnets, Phys. Rev. B **86**, 054409 (2012).

[60] C. P. Hofmann, Thermodynamics of two-dimensional ideal ferromagnets: Three-loop analysis, Phys. Rev. B **86**, 184409 (2012).

[61] K. Shen, Magnon Spin Relaxation and Spin Hall Effect Due to the Dipolar Interaction in Antiferromagnetic Insulators, Phys. Rev. Lett. **124**, 077201 (2020).

[62] L. R. Mead and N. Papanicolaou, Holstein-Primakoff theory for many-body systems, Phys. Rev. B **28**, 1633 (1983).

[63] M. M. Nieto and D. R. Truax, Holstein-Primakoff/Bogoliubov transformations and the multiboson system, Fortschr. Phys. **45**, 145 (1997).

[64] S. Halilov, A. Perlov, P. Oppeneer, and H. Eschrig, Magnon spectrum and related finite-temperature magnetic properties: A first-principle approach, Europhys. Lett. **39**, 91 (1997).

[65] S. Halilov, H. Eschrig, A. Y. Perlov, and P. Oppeneer, Adiabatic spin dynamics from spin-density-functional theory: Application to Fe, Co, and Ni, Phys. Rev. B **58**, 293 (1998).

[66] J. Als-Nielsen, O. W. Dietrich, and L. Passell, Neutron scattering from the Heisenberg ferromagnets EuO and EuS. II. Static critical properties, Phys. Rev. B **14**, 4908 (1976).

[67] D. Pushkarov and K. I. Pushkarov, Solitary magnons in one-dimensional ferromagnetic chain, Phys. Lett. A **61**, 339 (1977).

[68] G.-C. Wick, The evaluation of the collision matrix, Phys. Rev. **80**, 268 (1950).

[69] O. W. Dietrich, J. Als-Nielsen, and L. Passell, Neutron scattering from the Heisenberg ferromagnets EuO and EuS. III. Spin dynamics of EuO, Phys. Rev. B **14**, 4923 (1976).

[70] A. Bezuglyj, V. Shklovskij, V. Kruglyak, and R. Vovk, Temperature dependence of the magnon-phonon energy relaxation time in a ferromagnetic insulator, Phys. Rev. B **100**, 214409 (2019).

[71] V. Carteaux, D. Brunet, G. Ouvrard, and G. Andre, Crystallographic, magnetic and electronic structures of a new layered ferromagnetic compound $Cr_2Ge_2Te_6$, J. Phys.: Condens. Matter **7**, 69 (1995).

[72] G. Kresse and J. Furthmüller. Efficient iterative schemes for *ab initio* total-energy calculations using a plane-wave basis set. Phys. Rev. B **54**, 11169 (1996).

[73] L. Wang, T. Maxisch, and G. Ceder, Oxidation energies of transition metal oxides within the GGA+U framework, Phys. Rev. B **73**, 195107 (2006).

[74] S. Kang, S. Kang, and J. Yu, Effect of Coulomb interactions on the electronic and magnetic properties of two-dimensional $CrSiTe_3$ and $CrGeTe_3$ Materials, J. Electron. Mater. **48**, 1441 (2019).

[75] G. Menichetti, M. Calandra, and M. Polini, Electronic structure and magnetic properties of few-layer $Cr_2Ge_2Te_6$: The key role of nonlocal electron–electron interaction effects, 2D Mater. **6**, 045042 (2019).

[76] J. He, G. Ding, C. Zhong, S. Li, D. Li, and G. Zhang, Remarkably enhanced ferromagnetism in a super-exchange governed $Cr_2Ge_2Te_6$ monolayer via molecular adsorption, J. Mater. Chem. C **7**, 5084 (2019).

[77] K. Shen, Finite temperature magnon spectra in yttrium iron garnet from a mean field approach in a tight-binding model, New J. Phys. **20**, 043025 (2018).

[78] J. Barker and G. E. Bauer, Thermal Spin Dynamics of Yttrium Iron Garnet, Phys. Rev. Lett. **117**, 217201 (2016).

[79] Y. Liu and C. Petrovic, Critical behavior of quasi-two-dimensional semiconducting ferromagnet $Cr_2Ge_2Te_6$, Phys. Rev. B **96**, 054406 (2017).

[80] N. Ito, T. Kikkawa, J. Barker, D. Hirobe, Y. Shiomi, and E. Saitoh, Spin Seebeck effect in the layered ferromagnetic insulators $CrSiTe_3$ and $CrGeTe_3$, Phys. Rev. B **100**, 060402(R) (2019).

[81] D. Soriano, M. I. Katsnelson, and J. Fernández-Rossier, Magnetic two-dimensional chromium trihalides: A theoretical perspective, Nano Lett. **20**, 6225 (2020).

[82] L. Cornelissen, J. Liu, R. Duine, J. B. Youssef, and B. Van Wees, Long-distance transport of magnon spin information in a magnetic insulator at room temperature, Nat. Phys. **11**, 1022 (2015).

[83] L. J. Cornelissen, K. J. Peters, G. E. Bauer, R. Duine, and B. J. van Wees, Magnon spin transport driven by the magnon chemical potential in a magnetic insulator, Phys. Rev. B **94**, 014412 (2016).

[84] F. Bloch, Zur theorie des ferromagnetismus, Z. Phys. **61**, 206 (1930).

[85] D. R. Klein, D. MacNeill, J. L. Lado, D. Soriano, E. Navarro-Moratalla, K. Watanabe, T. Taniguchi, S. Manni, P. Canfield, and J. Fernández-Rossier, Probing magnetism in 2D van der Waals crystalline insulators via electron tunneling, Science **360**, 1218 (2018).